Contents lists available at ScienceDirect

Process Safety and Environmental Protection
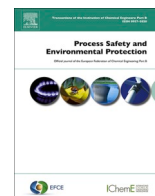
Biodiesel production from rapeseed oil over calcined waste filter cake from sugar beet processing

Jugoslav B. Krstić [a], Zvonko B. Nježić [b], Milan D. Kostić [c], Boško D. Marić [b],
Olivera D. Šimurina [b], Olivera S. Stamenković [c], Vlada B. Veljković [c, d, *]

[a] Institute of Chemistry, Technology, and Metallurgy, National Institute of the Republic of Serbia, University of Belgrade, Belgrade, Serbia
[b] Institute for Food Processing Technology in Novi Sad, University of Novi Sad, Serbia
[c] Faculty of Technology, Leskovac, University of Niš, Serbia
[d] Serbian Academy of Science and Arts, Belgrade, Serbia

ARTICLE INFO

ABSTRACT

A solid catalyst was prepared from waste filter cake (WFC) from a sugar beet processing plant and used, after calcination at 900 °C within 2 h, for biodiesel production from rapeseed oil and methanol. The calcined WFC (CFC) catalyst was characterized by XRF, FTIR, XRD, TGA/DTG, TPDe, TPD-CO₂, SEM, N₂ physisorption, and Hg porosimetry. The CFC is a CaO-based catalyst with a rigid, sustainable macroporous structure with the largest particles of 2.0×0.5 μm, a specific surface area of 7.3 m²/g, and a basicity of 0.27 mmol/g. It provides high conversion of 97.9% in 1 h at the methanol-to-oil molar ratio of 9:1, the temperature of 60 °C, and the catalyst loading of 10% of the oil mass. Its catalytic efficiency is comparable to the WFC-based nanocatalysts and CaO-based catalysts from natural sources. CFC was reused twice with a negligible decrease in catalytic activity, ensuring a FAME content above 97% in 1 h. The biodiesel produced from rapeseed oil over the CFC catalyst has good fuel properties that fulfill most of EN 14214. Therefore, WFC is a promising source of a low-cost, highly active, basic, and environmentally friendly CFC catalyst, which could reduce biodiesel production costs. From this point of view, this catalyst has great potential for developing the process at the commercial level.

1. Introduction

Biodiesel is a clean, renewable, biodegradable fuel used in diesel engines as pure or mixed with petrodiesel or ethanol. Transesterification is a primary process for biodiesel production, including the reaction between alcohol (mainly methanol) and an oily feedstock, usually catalyzed using a homogeneous or heterogeneous catalyst. Using heterogeneous catalysts eliminates many technological and environmental problems inherent to homogeneous catalysts (Živković et al., 2017). However, most developed heterogeneous catalysts are expensive or difficult to prepare, limiting their industrial application. This limitation can be overcome using natural or waste materials as heterogeneous catalysts. Therefore, extensive research has been conducted to develop commercially suitable and sustainable heterogeneous catalysts from inexpensive raw or waste materials, such as CaO-based catalysts.

Calcium oxide (CaO) is abundant in nature and industry in different forms, such as limestone (Sai Bharadwaj et al., 2020), dolomite (Ilgen, 2011; Ketcong et al., 2014; Ngamcharussrivichai et al., 2007; Shajaratun Nur et al., 2014), eggshells (Buasri et al., 2013; Jazie et al., 2013; Viriya-empikul et al., 2012), snail shells (Birla et al., 2012; Roschat et al., 2016), oyster shells (Nakatani et al., 2009), crab shells (Boey et al., 2009; Correia et al., 2014), biont (turtle) shells (Xie et al., 2009), bovine bone (Smith et al., 2013), palm kernel shells (Bazargan et al., 2015; Kostić et al., 2016), waste paper mill mud (Li et al., 2014), waste filter mud from sugar production (Abdelhady et al., 2020; Aghabarari and Martinez-Huerta, 2016), etc.

In the clarification stage of sugar production using calcium hydroxide, the sugar juice is separated into clear juice and filter mud. The former is used in sugar production, while the latter is further filtered to separate the suspended matter (fine plant particles and insoluble salts) as a filter cake. The yield of the wet filter cake is about 120 kg/t of sugar

---

* Corresponding author at: Faculty of Technology, Leskovac, University of Niš, Serbia.
E-mail addresses: jkrstic@nanosys.ihtm.bg.ac.rs (J.B. Krstić), zvonko.njezic@fins.uns.ac.rs (Z.B. Nježić), milan@tf.ni.ac.rs (M.D. Kostić), bosko.maric@fins.uns.ac.rs (B.D. Marić), olivera.simurina@fins.uns.ac.rs (O.D. Šimurina), stamenkovico@tf.ni.ac.rs (O.S. Stamenković), veljkovic@tf.ni.ac.rs (V.B. Veljković).

beet (Mishchenko et al., 2012). It typically contains 71% moisture, 20% volatile solids, 74–75% organic matter, and 9% ash (Agrawal et al., 2013). The main constituents of filter mud include 5–14% wax, 15–30% fiber, 5–15% crude protein, 5–15% sugar, 1–4% CaO, and 9–10% total ash (Partha and Sivasubramanian, 2006). Assuming a yield of 2% (Bhatnagar et al., 2016) and a total sugar beet production of 253 million tons in 2020 (Shahbandeh, 2022), global filter mud production is about 5 million tons. This waste filter cake (WFC) ages in natural conditions on open landfills while being decomposed microbially and washed by atmospheric precipitations; the complete decomposition and washing time is about 5–7 years. However, the sugar industry has problems managing, handling, and transporting WFC, so extensive efforts have been made to find its profitable uses. In agriculture, it is used as fertilizer (Yang et al., 2013), soil amendment (Shankaraiah and Murthy, 2005), and feed ingredient (Sahu et al., 2014). Its use as a resource includes biodiesel (Aghabarari and Martinez-Huerta, 2016; Remedios-Casta-ñeiras et al., 2019), biochar (Bernardino et al., 2017), and biogas (López González et al., 2014) production. Other uses are as a resource for wax production (Balakrishnan and Batra, 2011), heat generation (Oche-George et al., 2010), pyrolysis, combustion, or oxy-combustion (Da Silva et al., 2015), and cement and paint manufacturing (Yadav and Solomon, 2006). So far, wastes from sugar production like WFC have been used to prepare CaO-based nanocatalysts for biodiesel production (Abdelhady et al., 2020; Aghabarari and Martinez-Huerta, 2016).

This work deals with the preparation of a catalyst by calcination of WFC from sugar production from sugarbeets, called calcined filter cake (CFC), and its use in biodiesel production by the transesterification of rapeseed oil with methanol. The synthesized catalyst was characterized by X-ray fluorescence spectroscopy (XRF), Fourier Transform Infrared (FTIR), X-ray powder diffraction (XRD), temperature-programmed decomposition (TPDe), temperature-programmed desorption of CO$_2$ (TPD-CO$_2$), scanning electron microscope (SEM), low-temperature N$_2$ physisorption, and TGA (thermogravimetric analysis). Its catalytic activity and reusability were tested in rapeseed oil transesterification. Finally, the properties of the produced biodiesel were determined and compared with the biodiesel quality standard.

2. Experimental

2.1. Materials

2.1.1. Rapeseed oil

The rapeseed (*Brassica napus* subsp. *napus*) was obtained from (the Institute of Field and Vegetable Crops, Novi Sad, Serbia). The moisture content of the seeds was 2.1 ± 0.1 g/100 g. An oil screw press (Komet, Germany) with 8 mm nozzles was used to recover the oil from the rapeseed, which was then filtered under a vacuum to remove solid residues.

2.1.2. WFC

The WFC containing approximately 40% of moisture was taken from the landfill of the Crvenka Sugar Factory (Crvenka, Serbia), dried in a laboratory dryer with forced air circulation (Sutjeska, SFR Yugoslavia) at 98 °C for 60 min to about the moisture content of 10%, crushed by hands without tools, and sieved through a set of standard sieves (Endecotts Ltd., United Kingdom). A fraction smaller than 0.5 mm was further used for preparing the catalyst. The original WFC was gray-brown, while the dried powder was white.

2.1.3. Other chemicals

Methanol (99.5%) was from Zorka–Pharma (Serbia). HCl (36%) was purchased from Centrohem (Serbia), while HPLC grade *n*-hexane, 2–propanol, and methanol were purchased from Lab–Scan (Ireland). The HPLC standards for methyl esters and triacylglycerols were obtained from Sigma Aldrich (USA). CaCO$_3$ (ACS reagent, purity $\geq$99.0%) was purchased from Sigma-Aldrich. Na$_2$CO$_3$ and Na$_2$SO$_4$, both anhydrous, were supplied by Sigma Aldrich (USA). The HPLC standards for methyl esters of palmitic, stearic, oleic, and linoleic acids, trioleylglycerol, dioleylglycerol, and 1-oleylglycerol, all from Sigma Aldrich (USA), were used for external calibration.

2.2. Catalyst preparation and characterization

The dried WFC was calcined at 900 °C for 2 h, cooled to the ambient temperature, and stored in a dark glass bottle in a desiccator containing CaCl$_2$ and KOH until use.

The elemental composition of the CFC was determined in the helium atmosphere by the XRF analysis using a mobile ARTAX 200 μ-XRF spectrometer (BRUKER Nano, Germany) equipped with an Rh cathode ray tube and an integrated camera (25 kV, 1.5 mA). This device worked in the non-contact mode at 2 cm, where the inclination of the emitted X-ray was 45° to the tested surface, with a recording time of 100 s. The obtained spectra were analyzed using BRUKER's integrated ARTAX SPECTRA 7 software.

The FTIR spectra of WCF and CFC mud were recorded on a Thermo Nicolet 6700 FTIR spectrometer in the ATR technique using the Smart Orbit Diamond additive with a resolution of 4 cm^{-1} in the spectral range of 4000–400 cm^{-1}.

The XRD measurements were performed by a Rigaku Smartlab diffractometer equipped with a D/teX Ultra 250 strip detector using CuKα1,2 (U = 40 kV and I = 30 mA) with low-background single-crystal silicon sample holders. The measurement was conducted in the 2θ = 10–70° domain, step length of 0.01° and a rate of 5°/min.

Thermal properties of the WFC were analyzed by thermogravimetric analyzer (TGA) LECO TGA701 (LECO Corporation, St Joseph, MI, USA) in an airstream (3.5 L/min), with a heating rate of 10 °C/min in the range of 25–1000 °C.

The TPDe and TPD-CO$_2$ of the dried WFC and CFC samples, respectively, were performed using a TPDO 1100 device (Thermo Scientific) under the following conditions: 40–900 °C, 10 °C/min, and 20 cm^3 He/min, as described elsewhere (Veličković et al., 2021). The released and desorbed CO$_2$ amounts (from TPDe and TPD-CO$_2$, respectively) were determined by pulse calibration, considering the loop volume and the CO$_2$ concentration in the gas mixture. The correctness of calibration was confirmed by the TPDe of a CaCO$_3$ sample, denoted Std CaCO$_3$.

Morphology of the WFC and CFC was determined by a scanning electron microscope (SEM) (JEOL JSM-6610LV) equipped with a detector for detecting secondary and backscattered electrons (SEI and BEC, respectively).

The textural properties of the WFC and CFC samples were analyzed

by a Sorptomatic 1990 device (Thermo Finnigan). The results were processed using the software package ADP 5.13 (Thermo Electron). At the preparation place, the samples were, before measurement, vacuumed with heating at 110 °C for 24 h. The specific surface areas, micropore volume, and mesopore volume were estimated, as described elsewhere (Veličković et al., 2021).

The bulk density of the dried WFC and CFC samples was first determined using a Macropore Unit 120 (Fisons Instruments). Then, the mercury porosimetry was conducted in a high-pressure unit PASCAL 440 (Thermo Fisher) in the range of 0.1–200 MPa Hg, as described elsewhere (Veličković et al., 2021). Two consecutive intrusion-extrusion measurement cycles (Run1 and Run2) were performed for each measured sample. The control of the high-pressure unit and the collection, processing, and calculation of intrusion-extrusion measurement data were performed using the SOLID Ver software. 1.3.4 (Thermo Fisher).

2.3. Catalytic and reusability tests

2.3.1. Catalytic test

Appropriate amounts of the catalyst (CFC; 4%, 7%, and 10% of the oil weight) and methanol (methanol-to-oil molar ratio of 9:1) were first poured into a flask (250 mL). The mixture was thermostated for 30 min at 60 °C, and then 30 g of separately thermostated rapeseed oil was added. Next, a magnetic stirrer (900 rpm) vigorously agitated the reaction mixture, ensuring the space particle and composition uniformity. At various time intervals during the reaction, samples (0.5 mL) of the reaction mixture were taken and neutralized with an appropriate amount of HCl solution (concentration 5 mol/L) to stop the reaction. Next, the ester-oil and alcohol-aqueous phases were separated using a centrifuge (Sigma, Germany) at 3500 min^{-1} (average 700xg) for 15 min. Next, the upper ester-oil layer was separated, dissolved in a 1:200 mixture of 2-propanol: *n*-hexane (5: 4 v/v), filtered through a Millipore filter (0.45 μm), and analyzed by liquid chromatography (HPLC), as described elsewhere (Veličković et al., 2021). After the transesterification, the liquid part of the reaction mixture was first separated from the solid catalyst and then poured into a separatory funnel to separate crude biodiesel.

2.3.2. Reusability test

Catalyst reusability was tested under the following conditions: temperature of 60 °C, methanol-to-rapeseed oil molar ratio of 9:1, catalyst loading of 10%, and reaction time of 60 min. After the reaction, the solid catalyst was separated by filtration, washed with methanol, and reused without further pretreatment.

2.4. Analytical methods

2.4.1. HPLC analysis of the ester/oil phase

The chemical composition of the ester phase of the reaction mixture was determined by the HPLC method described elsewhere (Veličković et al., 2021). The external calibration curves, prepared using the standard mixture of fatty acid methyl esters (FAMEs) and the standard acylglycerols, were used to quantify the FAMEs and acylglycerols present in the samples analyzed. The weights of triacylglycerols (TAGs), diacylglycerols (DAGs), monoacylglycerols (MAGs), and FAMEs were calculated from corresponding peak areas using the calibration curves. The error of the FAME content determination in replicates was ± 1.0%. The HPLC chromatogram of a mixture of 1-oleylglycerol, methyloleat, 1, 2-dioleylglycerol, and trioleylglycerol is presented in Fig. S1.

2.4.2. Biodiesel characterization

The physicochemical properties of the purified biodiesel were measured using the standard methods: kinematic viscosity (EN ISO 3104:2003), density (EN ISO 3675:1988), water content (EN ISO 12937:2000), acid value (EN 14104:2003), iodine value (EN
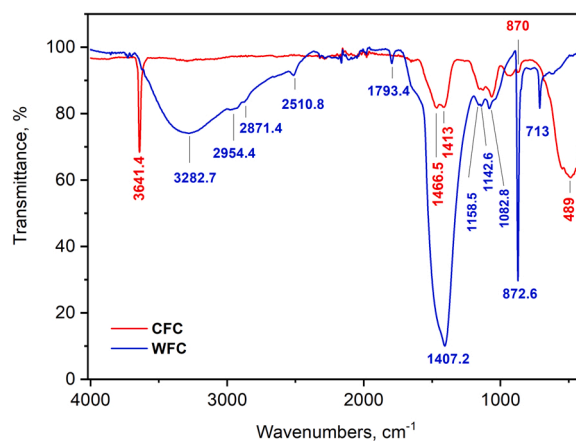

Fig. 1. FTIR spectra of WFC (blue) and CFC (red).

14111:2003), FAME content (EN 14103:2003), as well as acylglycerol contents (EN 14105:2003). Calcium was analyzed by atomic absorption spectrometry using a VARIAN SPECTRA AA10 Spectrophotometer. All measurements were conducted in duplicate.

3. Results and discussion

3.1. Catalyst characterization

3.1.1. Elemental composition of the CFC by XRF spectroscopic analysis

According to the XRF analysis, the CFC consisted mainly of calcium (90.23%), followed by magnesium (4.54%), silicon (1.46%), sulfur (1.31%), phosphorous (1.05%), and potassium (0.90%); aluminum (0.29%), iron (0,16%), strontium (0.05%), and manganese (0.01%) were among the detected trace elements. Besides moisture and the elements mentioned above, WFC usually contains wax, fiber, sugar, and trace amounts of other elements like zinc, copper, chromium, etc. (Bernardino et al., 2017; Partha and Sivasubramanian, 2006).

3.1.2. FTIR analysis

The FTIR spectra of WFC and CFC are shown in Fig. 1. The broad band observed in the region of large wave numbers of the WFC spectrum originates from the O–H stretching vibrations of adsorbed H$_2$O. On this band, two superposed low-intensity bands at about 2874 cm^{-1} and 2979 cm^{-1} from the C═O vibration of the CO$_3^{-2}$ anion are also noticeable. Further, the band with a minimum at 1795 cm^{-1}, originating from the C═O vibration of the CO$_3^{-2}$ anion, is observed. Finally, an intense, left-distorted band with a maximum at about 1407 cm^{-1} can be associated with the C–O vibration of the CO$_3^{-2}$ anion (Rodriguez-Blanco et al., 2011).

Based on the vibrations of the CO$_3^{-2}$ anion and a high amount of Ca (from the XRF analysis), it was concluded that CaCO$_3$ was dominant in the WFC. Asymmetry of the most intense band at 1466 cm^{-1} indicates a certain amount of amorphous CaCO$_3$, especially considering a band at 1083 cm^{-1}, which is associated with the stretching Ca═O vibrations from amorphous CaCO$_3$ (Shirsath et al., 2015). Besides the amorphous CaCO$_3$, calcite is the only present recognizable crystal CaCO$_3$ phase, as indicated by the presence of only two bands with minima at 873.6 cm^{-1} and 713 cm^{-1} and the absence of two bands at 855 cm^{-1} and 700 cm^{-1} (Ghiasi et al., 2020).

Despite the significant Mg content (4.6%) detected by the XRF measurement, the FTIR analysis could not confirm the presence of dolomite due to the absence of the bands at 730 cm^{-1} and 2626 cm^{-1} (Farmer, 1974; Ji et al., 2009; Nguyen et al., 1991). Finally, the low-intensity bands with the minimums in the 1160–1050 cm^{-1} region can originate from the organic components present in the WFC (C–O stretching and C–C bending from aromatics at 1158 cm^{-1} and
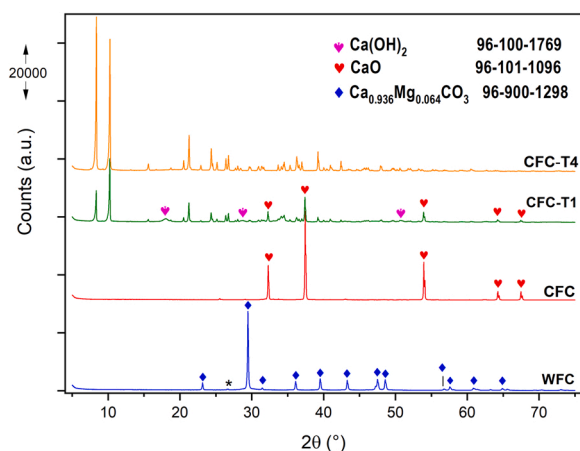
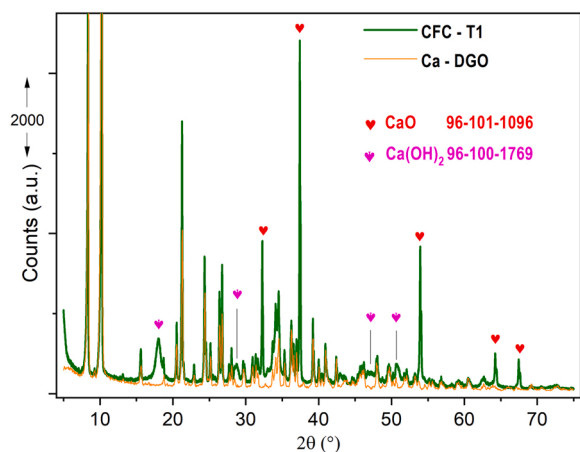**Fig. 2.** The XRD patterns of the WFC, CFC, and catalysts after Test 1 (CFC-T1) and Test 4 (CFC-T4).

Fig. 3. The XRD patterns of the catalyst after test 1 (CFC-T1) and the synthetized calcium diglyceroxide (Ca-DGO) sample.

1123 cm^{-1}, respectively, or C–O vibrations of the epoxy group at 1052 cm^{-1}) or some form of silicate species (Si-O stretching vibration from Si-O-Si-O or P–O–Si) (Khabbouchi et al., 2019).

The calcination process at 900 °C decomposes $CaCO_3$ from the WFC into CaO. The broad band on the CFC spectrum at about 490 cm^{-1} originates from the Ca–O vibrations, while bands at 1466 cm^{-1} and 870 cm^{-1} originate from the C–O vibrations. However, the same spectrum contains a sharp band with a minimum at about 3640 cm^{-1} (Fig. 1). This band is due to the hydrogen bonding of -OH groups, which is most probably associated with the existence of $Ca(OH)_2$, formed during the sample preparation for the measurement. In addition, there is no indication of a wide band of the physisorbed H_2O molecules due to their reaction with CaO forming $Ca(OH)_2$. The bands between 1160 cm^{-1} and 1050 cm^{-1} are slightly changed concerning the ratio of intensity and position compared to the corresponding bands in the WFC spectrum. Since all organic matter is removed during calcination, small changes imply that the silicate and organic material are present in the WFC, the organic phase content being lower.

3.1.3. XRD analysis

The XRD patterns of the WFC, CFC, and catalysts collected after the first and fourth catalytical tests are shown in Fig. 2. The diffraction pattern of the WFC resembles the diffractograms of the ordered calcite phase (Arma et al., 2014; Gregg et al., 2015; Kirboga et al., 2014; Luo et al., 2020; Sahebian et al., 2007), thus indicating it generally as
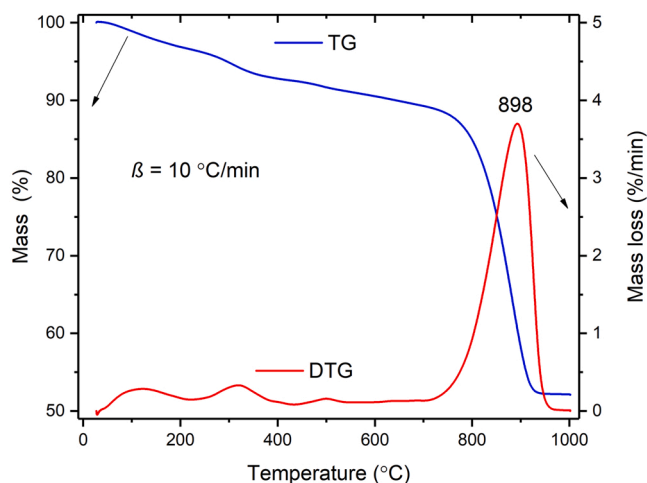

Fig. 4. TGA/DTG analysis of the WFC sample (air atmosphere, heating rate: 10 °C/min).

well-crystalline calcite with the absence of a CaO peak. However, it is almost impossible to distinguish the diffractograms of calcite and a chemically slightly different material, $Ca_{0.936}Mg_{0.064}CO_3$ (JCPDS card 96–900–1298), also referred calcite, at least for the applied XRD data collection conditions. Considering the XRF analysis and Match 3! pattern recognition software, two possible calcite phases (96–900–1298 and 96–900–0967) were founded in a ratio of 3:1 in the XRD pattern of the WFC. Also, a small unidentified peak, denoted with symbol * at 2θ $\approx (26.62 \pm 0.04)°$ in Fig. 2, can be recognized as SiO_2 (JCPDS card 96–153–6390), or even $Ca_2Mg_{0.96}Si_2O_7$ (JCPDS card 96–900–6117) with a contribution of less than 1%. The diffractogram peaks confirm that the CFC is almost entirely made of CaO formed by calcinating calcite from the WFC. Both the positions (2θ = 32.3, 37.4, 53.9, 64.3, and 67.5) and the intensities of the diffraction peaks characterize the crystallized structure of CaO and coincide with those on the JCPDS card 96–101–1096. Other phases, including MgO, were not registered.

The diffractogram changes significantly after the first catalytic test (CFC-T1) compared to the fresh CFC (Fig. 3). A new phase (or phases) appears as indicated by many new peaks, two of which are most pronounced at 2θ $\approx 8.3°$ and 10.2°. Furthermore, the intensities of the signals in the CFC-T1 diffractogram originating from CaO are significantly reduced. Low-intensity reflections, which arose from $Ca(OH)_2$ (JPDCS card 96-100-1769), indicated that during the catalytic reaction, a part of CaO was transformed into $Ca(OH)_2$. However, the amount of the formed $Ca(OH)_2$ was insufficient to explain the significant reduction in the CaO signal.

The positions of the two most intense peaks indicate the possible existence of calcium diglyceroxide (Ca-DGO) in the CFC-T1 sample (Chen et al., 2020; Puna et al., 2014). The diffractograms of the Ca-DGO sample, synthesized by the method of Fujii and Kondo (1968), and the CFC-T1 sample are given in Fig. S2 (Supplementary Material). A simple comparison of the positions of the peaks leaves no doubt that the phase formed during the catalytic test is Ca-DGO. Hence, the reflection intensity in the CFC-T1 diffractogram connected to CaO is reduced compared to the CFC diffractogram due to the Ca-DGO formation. Finally, the diffractogram of the materials collected after the fourth catalytic test (CFC-T4) has the reflections originating exclusively from the Ca-DGO phase (Fig. S2, Supplementary Material). In the CFC-T4 sample, there is no evidence of CaO, $Ca(OH)_2$, and any other phase identified in the CFC-T1 sample.

3.1.4. TGA/DTG analysis

The thermal decomposition of the WFC under an oxidation atmosphere was investigated by simultaneous thermogravimetry (TG) and derivative thermogravimetry (DTG). The TG measurement gives a
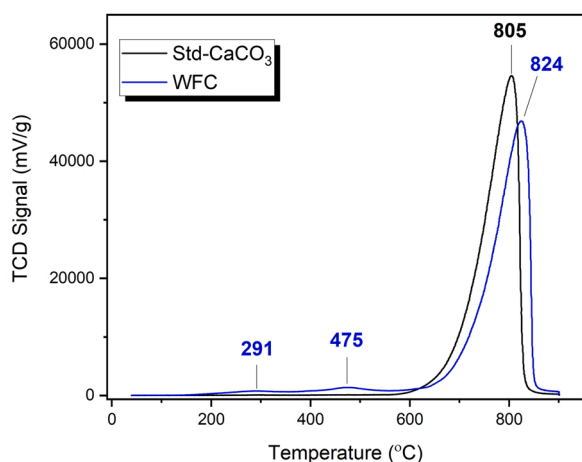
Fig. 5. The TPDe profiles of the WFC (blue) and CaCO₃ standard (black) samples.
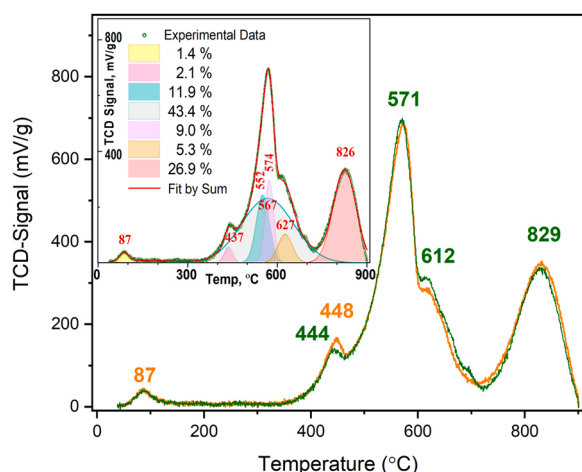

Fig. 6. TPD-CO₂ profiles of TCD signals of two CFC samples; Insert - deconvolution curves, values of their temperature maxima, and percentage of individual components in the filtered profile (Fit by Sum).

temperature curve typical for the thermal decomposition of $CaCO_3$ to CaO in an air atmosphere, with one peculiarity – deviation from the horizontal line in the TG signal up to 600 °C (Fig. 4). This deviation is related to water, organic matter, and even $MgCO_3$ in the WFC sample. The mass-loss rate is not the same in regions of low and high temperatures. It changes slowly up to 600 °C, and the total weight loss does not exceed 11.5%. A drop in mass in the temperature range of 600–910 °C corresponds to the release of CO_2 from the calcite phases. Calcination is still slow at the beginning of this interval, then increases rapidly, reaches a maximum of 898 °C, and then falls sharply to zero above 910 °C. The mass of the sample remains unchanged above this temperature, which indicates that the WCF degradation is complete. The analysis revealed a mass loss of about 49,8%, significantly higher than the theoretical value for pure calcite (44.0%). At least 3% of the mass loss comes from H_2O desorption during the first 200 °C of heating, and the rest results from burning or calcinating other unidentified constituents.

3.1.5. TPDe characterization of WFC and TPD-CO₂ measurement of CFC

The TCD profiles of the TPDe measurement for the WFC and standard $CaCO_3$ material (Std CaCO₃) are shown in Fig. 5, while two TCD profiles of the TPD-CO₂ measurement for the CFC samples are presented in Fig. 6. All signals were normalized per unit mass of the tested material. Therefore, the areas below the curves could be treated as an absolute

measure of the events due to decomposition (TPDe measurements) or CO_2 desorption (TPD-CO₂ measurements).

The differences in the TPDe profiles of the WFC and Std-CaCO₃ samples, although not significant, are noticeable (Fig. 5). The WFC sample has two small, low-temperature signals with maxima at about 290 °C and 475 °C, which do not exist in the TCD profile of the Std-CaCO₃ sample, where the baseline is entirely straight. Since the pre-treatment of both samples is the same, these differences originate from decomposing the organic and other impurities in the WFC sample.

A more noticeable difference refers to the position of the dominant maxima, which shifts by about 20 ºC towards higher temperatures for the WFC sample. In addition, although the shape of the high-temperature profiles of both materials is the same (growth after 620 ºC, reaching the maximum above 800 ºC, and an almost vertical drop to the baseline at 840–850 ºC), the areas below the two curves are not. The area below the high-temperature part of the WFC signal corresponds to 91.2% of the total area below the Std CaCO₃ sample signal, confirming that the WFC is not pure calcite. Even when the area of the two low-temperature peaks is considered, the total area under the WFC sample curve is about 97.5% of the entire area. It means the non-calcite parts of the WFCs do not contain carbon or oxygen (or both), or they are in the form of compounds with a mass fraction lower than that in calcite. Due to the maximum position, the peak's width, and the signal's return to the baseline, the temperature of 900 ºC is sufficient for the complete calcination of the WFC sample.

The TPD-CO₂ measurements were performed to determine the amount and strength of the basic sites of CFC. The obtained TCD profiles of the two CFC samples, which differed in their initial mass, are shown in Fig. 6. Also, two measurements were performed to verify the method's reproducibility. The remarkable resemblance of the profiles, including the positions of the peaks, intensities, and the total area below curves (2% difference), confirms the repeatability of the measurements and the accuracy of the determined total specific amount of the basic sites.

For the CFC, the classification of temperature intervals, suggested by Viriya-empikul et al. (2012) for the TPD-CO₂ analysis of Ca-based catalysts obtained from industrial waste, was accepted. The total basicity of the CFC sample is a combination of medium and strong base sites, as the signal almost exclusively belongs to temperatures above 400 °C (Insert Fig. 6). Indeed, less than 2% of the total area below the TPD-CO₂ curve belongs to the area of the weakly binding sites, which, according to the vast majority of literature data, are not significant for the biodiesel synthesis reaction. However, taking into account the parts of individual deconvolution curves for the temperature ranges 400–550 °C and above 550 °C, the share of the strong basic sites is about three times higher than that of the medium basic ones. The origin of the medium strength site is usually associated with the presence of the Ca–O ion pairs in materials CFC. However, it is evident from the insert in Fig. 6 that the CO_2 adsorption sites of similar origin also exist in the CFC above 550 °C, up to 700 °C. So, the Ca–O ion pairs (medium-strong sites) also contribute to the signal in the high-strength site region.

A qualitatively different contribution to the TPD-CO₂ profile is given by the part of the signal above 700 °C, which makes up 30% of the total basic sites present in the CFC sample. It is a consequence of the desorption of CO_2 from the high-strength sites (actually O^{2-} anions) that are present on the surface of the CFC sample. These anions have a free electron pair (which makes them Lewis bases), and since the CO_2 molecule is a Lewis acid, due to the existence of double bonds between atoms of different electronegativity, a strong bond formed between them can be broken only at high temperatures.

Besides the type of basic sites present on the catalyst surface, the total specific amount of basic sites is expressed as the mean value of the two measurements (272 ± 3 µmol/g). Compared to the literature data, the content of base centers of the CFC is higher than those of calcined eggshells, river snail shells, and golden apple snails but smaller than the values for commercial CaO (Roschat et al., 2018).
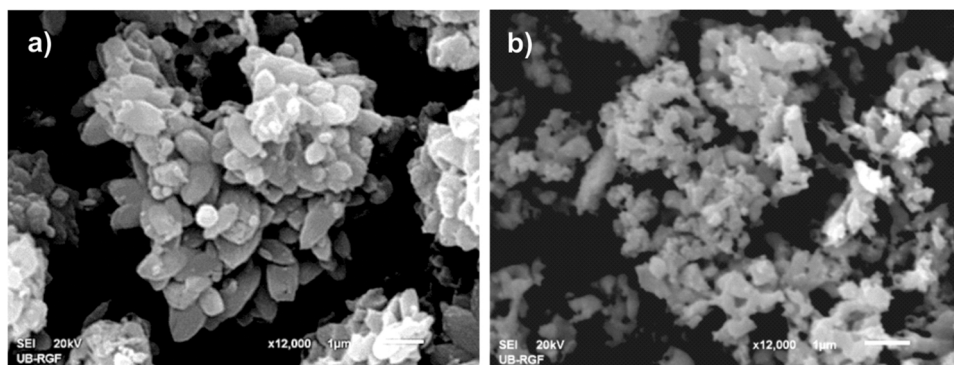
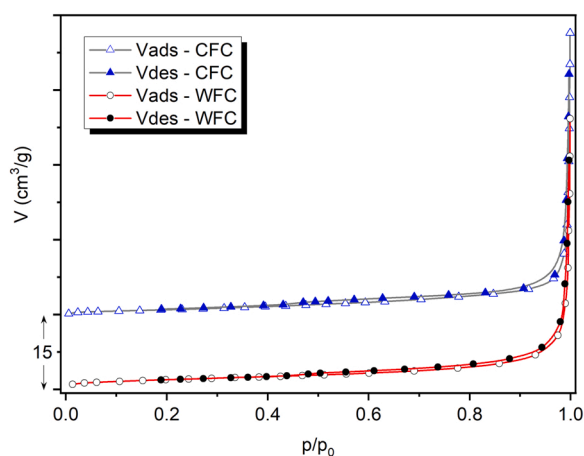**Fig. 7.** The WFC (a) and CFC (b) samples, magnification 12,000x.

Fig. 8. The N_2 isotherms of the WFC and CFC samples (the CFC isotherm translated for 15 cm^3/g).

Table 1

Textural characteristics of the WFC and CFC samples (physisorption of N_2 at 77 K).

Measured characteristic		Type of sample	
		WFC	CFC
Total pore volume (Gurvich method)[a]	V_{tot}, cm^{3}g^{-1}	0.020	0.016
Specific surface area (BET method)	S_{BET}, m^{2}g^{-1}	7.1	7.3
	C_{BET}	60	293
Mesopore volume (BJH method)	V_{meso}, cm^{3}g^{-1}	0.015	0.012
	S_{meso}, m^{2}g^{-1}	5.7	6.3
Micropores volume (Dubinin and Raduskevich method)	V_{mic}, cm^{3}g^{-1}	0.003	0.003

[a] The value of V_{tot} determined for p/p$_0$ = 0.98.

3.1.6. Morphology SEM analysis

Fig. 7 shows 12,000x magnification SEM micrographs for the WCF and CFC samples. Syntheses of CaCO$_3$ with a long-precipitated time usually result in a recognizable shape of the rhombohedral structure of calcite (Liu and Yates, 2006; Ševčík et al., 2018). However, this form cannot be identified on the WCF micrographs. It is not surprising, considering at least two things. First, calcite has trigonal symmetry allowing more than 300 characteristic external shapes (Dietrich, 2013), including flatter or acute rhombohedral crystal habits, prismatic, sca-lenohedral, and tabular ones. Second, the influence of various sub-stances and physicochemical conditions as shape modifiers of CaCO$_3$ during the precipitation process has been well documented in the literature (Fernandez-Diaz et al., 1996; Kim et al., 2017, 2021; Paquette and Reeder, 1995; Reddy and Hoch, 2012). So, it would not be unex-pected if the morphology of WFC was predetermined by the various organic components or cations present in the initial slurry mixture and different unknown physicochemical conditions present in the disposal and storage stages of the WFC. Whatever the reason, SEM micrography of the WFC is dominated by clustered structures composed mainly of elongated and slightly pointed ellipsoidal particles. The largest di-mensions are 2 µm along the longer axis and 0.8 µm along the shorter axis, and there are also significantly smaller particles.

The SEM image of the CFC sample reveals significantly smaller particles than those of the WFC sample (Fig. 7a). The observed morphological changes are associated with the CO$_2$ release and the combustion of the organic phase present in the WCF during the calci-nation process. On a CFC micrograph, the largest particles along the shorter axis do not pass 0.5 µm and are no longer than 2 µm. Also, there are a lot of smaller particles, but their dimensions cannot be precisely

determined for the applied magnification. It seems that a significant number of CFC particles are in contact forming a particular 3D (pseudo) network of possible rigid structures, which will increase the porosity of the CFC sample relative to the WCT sample.

3.1.7. N_2 physisorption

The CFC and WCF samples were characterized using low-temperature N_2 physisorption and Hg porosimetry to determine the textural property changes caused by calcination. The N_2 physisorption isotherms at 77 K of WFC and CFC samples are shown in Fig. 8, while the obtained textural parameters of both materials are given in Table 1. For clarity reasons, the isotherm of the CFC sample is shifted up to a 15 cm^3/g. According to IUPAC nomenclature (Thommes et al., 2015), the ob-tained isotherms of both samples are the II type, a characteristic of macroporous and non-porous materials.

The starting material has a small specific surface area and a specific volume of micropores and mesopores. As the isotherm does not have a plateau at high relative pressure, a necessary characteristic for accu-rately determining the total pore volume, the value of V_{tot} in Table 4 must be taken with precaution. Small S_{BET} values of the WFC sample are not uncommon for CaCO$_3$, obtained in the laboratory (Bang et al., 2012; Ghiasi et al., 2020) or the industry (Dazon et al., 2019), with particles that are not nanometer-sized.

The calcination of the initial sample did not cause significant changes in the measured textural values. Therefore, the increase in the specific surface area is hardly measurable. Nevertheless, the obtained value agrees with the earlier reported specific surface area of 7 m^2/g for a CaO sample obtained by calcining CaCO$_3$ (Gullett et al., 1988).

Small changes in the S_{BET} value of the CFC compared to the value for WFC show that they occur in the range of pores with a small contribution to a specific surface area. In other words, morphological changes that have undoubtedly been identified on SEM micrographs are in the range of pore dimensions that do not affect the change in the specific surface
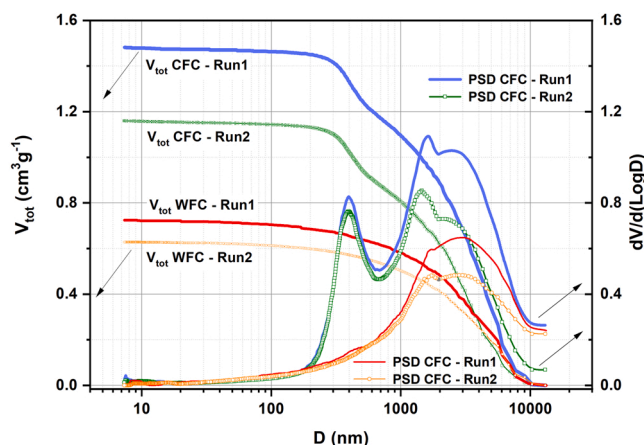
Fig. 9. Total intruded volume of Hg (V_{tot}) and pore size distribution of the WCF and CFC samples for two consecutive runs (Run1 and Run2).

area of the material. Therefore, it means that a possible CFC catalytic activity change compared to the WFC activity must originate from a change in surface chemistry.

3.1.8. Hg porosimetry

Hg porosimetry measurements can help overcome the open questions about WFC and CFC textural characteristics, such as non-porous or macroporous nature, the actual value of total pore volume, etc. Therefore, both samples were subjected to two consecutive intrusion-extrusion measurement cycles (designated Run1 and Run2) to assess the contribution of interparticle and intraparticle space. Namely, during the first intrusion cycle, the mercury can fill up both the interparticle (voids) and intraparticle spaces (pores) of the powder materials. In contrast, in the second intrusion cycle, Hg can occupy only the space of the accessible pores (Emeruwa et al., 1991). The intrusion Hg curves as a total intruded volume of Hg for Run1 and Run2 and the corresponding pore size distribution curves for the WFC and CFC samples are shown in Fig. 9.

Based on the first intrusion-extrusion measurement (Table 1 - Run1), it is clear that WFC has a significant value of the total specific pore volume (0.725 cm³/g). The relatively narrow hysteresis of the intrusion-extrusion curve (Fig. S3, Supplementary Material) and a slight reduction in the total intruded mercury volume (V_{tot-Hg}) between Run1 and Run 2 (about 13%) show that the porosity measured in Run 1 originates predominantly from the actual pores due to the stable organization of the building particles in the agglomerates that were identified on the SEM micrographs. These agglomerates do not disintegrate or collapse even under the action of the highest applied pressures (i.e., 2000 bar) during the Hg intrusion process. The pore size distribution curves confirm this view of WFC (Fig. 9). The maxima on the pore size distribution (PSD) curve remain at almost unchanged positions (about 3 μm) for Run 2 compared to Run1, and the total porosity reduction is less than 4% (Table 2). Therefore, it is not surprising that the total porosity

determined by the Hg porosimetry in Run2 is significantly preserved and reaches 60%. However, the determined specific surface area in both measurement cycles is below the values determined by N_2 phys-isorption. It means that a significant part of the specific surface area of the WFC sample originates from the pore diameter smaller than the lower detection limits of Hg porosimetry (7.5 nm for the applied maximal pressure).

The calcination of the initial WFC results in visible changes in the intrusion profile (Figs. 8 and S3 – Supplementary Material), and the numerical values testify to a twofold increase in the total mercury volume intruded in Run 1 (Table 2). Although the value of V_{tot} for Run 2 decreases by slightly more than 20%, which corresponds to the share of interparticle porosity, the total value remains high and reaches 1.16 cm³/g. Also, compared to the Run 2 starting material, the V_{tot} of the CFC sample is still 1.8 times higher, and its high porosity value can be beneficial in its application in a heterogeneous catalytic system.

The introduction of Hg into a powder sample by a constant increase in pressure during Run 1 can rearrange the sample particles' organization by the compaction mechanism and create systems of voids that are not present in the starting material. Still, they will be registered as a pore system with a further pressure increase when Hg fills this space. Although such a scenario cannot be completely ruled out for measuring a CFC sample, it is unlikely for at least two reasons. The first one concerns the pore distribution and peak positions for the dimensions greater than 1 μm, which agree with the measurements for the starting material. This behavior is unexpected for the porosity caused by mercury penetration, considering that materials with different particle dimensions are expected to have various distributions of the induced pore system. Furthermore, Hg intrusion-induced porosity is unlikely as different particle dimensions have been recognized in the WFC and CFC SEM
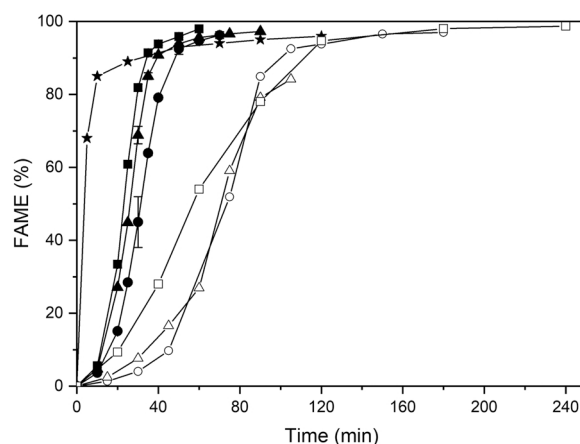

Fig. 10. Influence of the CFC catalyst amount (4% – ●, 7% – ▲, and 10% – ■) on FAME content at the methanol-to-rapeseed oil molar ratio of 9:1 and 60 °C and comparison with palm kernel shell biochar (5%) – ○, neat CaO (5%) – Δ (Bazargan et al., 2015), biont shell catalyst (70 °C, 3%, 9:1) – □ (Xie et al., 2009), and KOH (60 °C, 1%, 6:1) – ★ (Rashid and Anwar, 2008).

Table 2
Parameters calculated from Hg porosimetry measurements for WFC and CFC.

Sample	V_{tot-Hg}[a] (cm³/g)		ρ_{app}[b] (g/cm³)		ρ_{bulk}[c], (g/cm³)		SSA_{Hg}[d] m²/g		Porosity (%)	
	Run1	Run2	Run1	Run2	Run1	Run2	Run1	Run2	Run 1	Run2
WFC	0.725	0.629	2.38	3.27	0.87	0.95	5.1	3.9	63.3	60.0
CFC	1.482	1.160	2.38	3.27	0.56	0.68	8.8	7.5	82.9	79.1

[a] Total intruded Hg volume was obtained for the pressure of 200 MPa.
[b] Apparent density obtained by Hg porosimetry for the pressure of 200 MPa.
[c] Bulk density obtained by Hg picnometry for the atmospheric pressure.
[d] Specific surface area obtained for a cylindrical pore model.

Table 3

An overview of CaO-based catalysts obtained from wastes used in transesterification reactions.

Catalyst source / Active species	Calcination temperature (°C) / time (h)	Feedstock	Transesterification conditions			Fame yield (conversion) (%) / time (h)	Ref.
			Methanol:oil ratio (mol/mol)	Temperature (°C)	Catalyst loading (% of oil mass)		
WFC[a]	900 /2	Rapeseed oil	Methanol / 9:1	60	10 7 4	(97.9) / 1 (97.3) / 1.5 (97.1) / 1.5	This work
WFC[b]	900 / 2	Canola oil	12:1	60	5	(96) / 1.5	Aghabarari and Martinez-Huerta (2016)
WFC[c]	800 / 2	Sunflower oil	4.5:1	75	1	(93) / 1	Abdelhady et al. (2020)
Waste paper mill mud	800 / -	Peanut oil	15:1	64	6	(94) / 6	Li et al. (2014)
Limestone (CaCO$_3$) / CaO	900 / 4	Rubber seed oil	12:1	65	4	(95.2) / 5	Sai Bharadwaj et al. (2020)
Waste eggshells / CaO	800 / 2–4	Palm oil	18:1	60	10	94 / 2	Viriya-empikul et al. (2012)
Waste chicken eggshells / CaO	600–800 / 4	Palm oil	9:1	65	20	(94) / 3	Buasri et al. (2013)
Waste duck eggshells / CaO	600–800 / 4	Palm oil	9:1	65	20	(92) / 3	Buasri et al. (2013)
Waste eggshells / CaO	900 / 2	Rapeseed oil	9:1	60	3	96 / 3	Jazie et al. (2013)
Snail shells / CaO	900 / 3.5	Waste frying oil	6.03:1	60	2	99.6 / 8	Birla et al. (2012)
Snail shells / CaO	600–1000 °C / 3 h	Palm oil	12:1	65	5 (plus 10% THF)	98.5 / 1.5	Roschat et al. (2016)
Oyster shells / CaO	1000 / 3	Soybean oil	6:1	65	25	73.8 (98.4) / 5	Nakatani et al. (2009)
Crab shells / CaO	900 / 2	Sunflower oil	6:1	60	3	(83) / 4	Correia et al. (2014)
Waste venus clam	900 / 6	Palm oil, refined	15:1	65	5	97 / 6	Syazwani et al. (2017)
Mudcrabe (*Scylla serrata*)/ CaO	900	Palm olein oil	0.5:1	65	5	95 /2.5	Boey et al. (2009)
Bovine bone	750 / 6	Soybean oil	6:1	65	8	97 / 2	Smith et al. (2013)
Biont (turtle) shells / KF-CaO	300 /	Rapeseed oil	9:1	70	3	97 / 3	Xie et al. (2009)
Dolomite (CaMg(CO$_3$)$_2$) / CaO+MgO	800 / 4	Palm kernel oil	30:1	50	Continuous	86.5 / 2	Ketcong et al. (2014)
		Deodorized palm oil	30:1	60		93.2 / 2	
		Palm olein oil	50:1	60		92.3 / 2	
		Waste cooking oil	50:1	60		86.5 / 2	
Dolomite (CaMg(CO$_3$)$_2$) / CaO+MgO	900 / 8	Palm oil	15:1	65	1	(100) / 4	Shajaratun Nur et al. (2014)
Dolomite (CaMg(CO$_3$)$_2$) / CaO+MgO	800 / 2	Palm kernel oil	30:1	60	6	(98) / 3	Ngamcharussrivichai et al. (2007)
Dolomite (CaMg(CO$_3$)$_2$)	850 / 2	Canola oil	30:1	60	15.6	(100) / 4	Ilgen (2011)

[a] Particle size: < 2000 × 800 nm, specific surface area: 7.3 m^2/g, basicity: 0.272 mmol/g.
[b] Particle size: 100 nm, specific surface area: 25.1 m^2/g, basicity: 13.7 mmol/g.
[c] Particle size: 33 nm, specific surface area: 27.9 m^2/g, basicity: strong.

micrographs. The second concerns a peak at about 400 nm in both Hg intrusion measurement cycles of the CFC sample. Its stable position, which corresponds to a pressure of around 38 bars, would be difficult to maintain given that the maximum applied pressure was 2000 bars.

Based on all the above, it is possible to give answers to the questions that remained open after the analysis of physisorption using N$_2$ and SEM micrographs. Both materials can be classified as macroporous, considering the high values of the determined porosities. Also, the CFC with a rigid, sustainable macroporous structure developing an additional porosity is formed during the WFC calcination.

High porosity values (almost 80% for Run2) of the CFC sample and favorable pore distribution indicate the possibility of full utilization of surface-active centers, i.e., the absence of possible diffusion limitations during the catalytic TAG transformation to biodiesel.

3.2. Production of biodiesel from rapeseed oil in the presence of CFC

3.2.1. Comparison of the catalytical activities of CFC and other catalysts

Alkali hydroxides and CaO-based catalysts are among the most frequently used catalysts for transesterifying vegetable oils. Therefore, it is encouraging to compare the efficiencies of the rapeseed oil transesterification catalyzed with traditional and CaO-based catalysts. Fig. 10 illustrates the progress of the rapeseed oil transesterification over CFC (this work), KOH (Rashid and Anwar, 2008), neat commercial CaO, and CaO-based catalysts like palm kernel shell biochar (Bazargan et al., 2015), and biont shell catalyst (Xie et al., 2009). KOH is more efficient in the initial stage of the reaction than the solid ones because of no mass transfer limitations in the homogeneous system. On the other hand, besides the mass transfer limitation between the two immiscible liquids, the heterogeneous catalysis rate can be controlled by intraparticle and external liquid-solid mass transfer limitations (Veljković et al., 2009). However, a higher FAME content was achieved in the final equilibrium stage of the reactions catalyzed by CaO-based catalysts. Therefore, the observed difference in the efficacy of the two solid catalysts might be due to different loadings.

Table 3 compares the reported CaO-based catalysts derived from WFC and other natural sources used in the transesterification reactions. For example, Aghabarari and Martinez-Huerta (2016) and Abdelhady
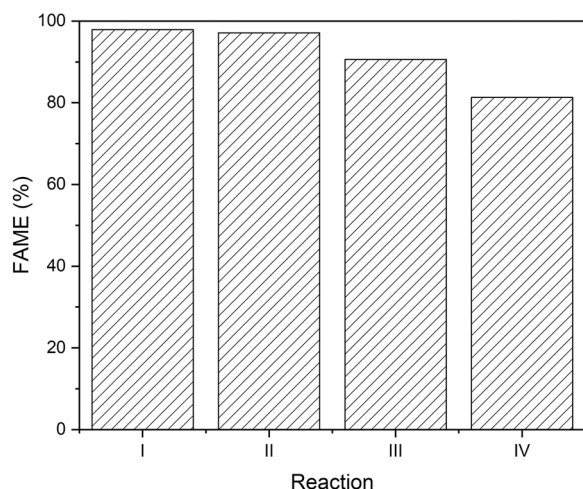
Fig. 11. The variation of FAME content in four consecutive reaction cycles (60 °C, the methanol-to-oil molar ratio of 9:1, the catalyst loading of 10 wt%, and the reaction time of 60 min).

Table 4
The physicochemical properties of the obtained biodiesel after purification.

Property	CFC	EN 14214
Density (15 °C), kg/m^3	882	860–900
Viscosity (40 °C), mm^2/s	4.1	3.5–5.0
Acid value, mg KOH/g	0.43	0.50 max
Iodine value, g I$_2$/100 g	106	120 max
Water, mg/kg	312	500 max
Ca+Mg, ppm	960	5
FAME, %	98.6	96.5 min
MAG, %	0.8	0.8 max
DAG, %	0.4	0.2 max
TAG, %	0.2	0.2 max

et al. (2020) used CFC-nanocatalysts to transesterify canola and sunflower oil with a conversion of 96% in 1.5 h and 93% in 1 h, respectively, under somewhat different reaction conditions. Although the CFC catalyst prepared in the present study had larger particles with a smaller specific surface area and lower basicity, a higher conversion (97.9% in 1 h) was achieved compared to the previous two studies. This conversion is also higher than those achieved with other CaO-based catalysts such as waste eggshells, crab shells, bovine bones, and paper mill mud combined with palm, sunflower, soybean, and peanut oil, respectively (Table 3).

3.2.2. Catalyst reusability
Results for four consecutive reaction cycles are given in Fig. 11. The CFC was reused twice with a negligible decrease in catalytic activity, with FAME content of 97.9% and 97.1% achieved in 1 h in the first two cycles. After that, however, the calcium content in the crude biodiesel of 960 ppm indicated significant leaching of the calcium species.

3.2.3. Biodiesel physicochemical properties
Some physicochemical properties of the biodiesel obtained by the rapeseed oil methanolysis over CFC are presented in Table 4. All the tested properties fulfill the standard specification except the calcium and DAG contents, thus indicating the need for additional biodiesel purification. The calcium leaching during the reaction is a known disadvantage of CaO-based catalysts, which can be overcome by adequate biodiesel purification (Kostić et al., 2016).

4. Conclusion

WFC, waste from sugar beet processing, is a very active basic catalyst

after calcination (900 °C, 2 h) in the transesterification of rapeseed oil under relatively mild reaction conditions (methanol-to-oil molar ratio of 9:1, temperature of 60 °C, and catalyst loading of 4–10%), ensuring a high oil conversion of 97.9% in 1 h. Therefore, it can be used as a low-cost and environmentally friendly source of CaO-based heterogeneous catalysts for producing biodiesel from rapeseed oil by a "green" process, reducing its costs. The high catalytic activity of the CFC catalyst is comparable to the activities of other CaO-based catalysts prepared from the WFC and natural sources. The biodiesel produced from rapeseed oil over the CFC had good fuel properties, which compile the specifications set by EN 14214.

Declaration of Competing Interest

The authors declare that they have no known competing financial interests or personal relationships that could have appeared to influence the work reported in this paper.

Acknowledgments

Appendix A. Supplementary material

Supplementary data associated with this article can be found in the online version at doi:10.1016/j.psep.2022.10.021.

References

Abdelhady, H.H., Elazab, H.A., Ewais, E.M., Saber, M., El-Deab, M.S., 2020. Efficient catalytic production of biodiesel using nano-sized sugar beet agro-industrial waste. Fuel 261, e116481. https://doi.org/10.1016/j.fuel.2019.116481.
Aghabarari, B., Martinez-Huerta, M.V., 2016. Biodiesel production using calcined waste filter press cake from a sugar manufacturing facility as a highly economic catalyst. J. Am. Oil Chem. Soc. 93, 773–779. https://doi.org/10.1007/s11746-016-2829-2.
Agrawal, K.M., Barve, B.R., Khan, S.S., 2013. Biogas from pressmud. IOSR J. Mech. Civ. Eng. 37–41.
Arma, L.H., Saitoh, A., Ishibashi, Y., Asahi, T., Sueoka, Y., Sakakibara, M., Takebe, H., 2014. Red fluorescence lamellae in calcitic prismatic layer of *Pinctada vulgaris* shell (Mollusc, bivalvia). Opt. Mater. Express 4, 1813–1823. https://doi.org/10.1364/OME.4.001813.
Balakrishnan, M., Batra, V.S., 2011. Valorization of solid waste in sugar factories with possible applications in India: a review. J. Environ. Manag. 92, 2886–2891. https://doi.org/10.1016/j.jenvman.2011.06.039.
Bang, J.-H., Jang, Y.N., Kim, W., Song, K.S., Jeon, C.W., Chae, S.C., Lee, S.-W., Park, S.-J., Lee, M.G., 2012. Specific surface area and particle size of calcium carbonate precipitated by carbon dioxide microbubbles. Chem. Eng. J. 198, 254–260. https://doi.org/10.1016/j.cej.2012.05.081.
Bazargan, A., Kostić, M.D., Stamenković, O.S., Veljković, V.B., McKay, G., 2015. A calcium oxide-based catalyst derived from palm kernel shell gasification residues for biodiesel production. Fuel 150, 519–525. https://doi.org/10.1016/j.fuel.2015.02.046.
Bernardino, C.A.R., Romeiro, G.A., 2017. Preparation of biochar from sugarcane by-product filter mud by slow pyrolysis and its use like adsorbent. Waste Biomass Valoriz. 8, 2511–2521. https://doi.org/10.1007/s12649-016-9728-5.
Bhatnagar, A., Kesari, K.K., Shurpali, N., 2016. Multidisciplinary approaches to handling wastes in sugar industries. Water Air Soil. Pollut. 227, e11 https://doi.org/10.1007/s11270-015-2705-y.
Birla, A., Singh, B., Upadhyay, S., Sharma, Y., 2012. Kinetics studies of synthesis of biodiesel from waste frying oil using a heterogeneous catalyst derived from snail shell. Bioresour. Technol. 106, 95–100. https://doi.org/10.1016/j.biortech.2011.11.065.
Boey, P.-L., Maniam, G.P., Abd Hamid, S., 2009. Biodiesel production via transesterification of palm olein using waste mud crab (*Scylla serrata*) shell as a heterogeneous catalyst. Bioresour. Technol. 100, 6362–6368. https://doi.org/10.1016/j.biortech.2009.07.036.
Buasri, A., Chaiyut, N., Loryuenyong, V., Wongweang, C., Khamsrisuk, S., 2013. Application of eggshell wastes as a heterogeneous catalyst for biodiesel production. Sustain. Energy 1, 7–13. https://doi.org/10.12691/rse-1-2-1.

Chen, X., Li, Z., Chun, Y., Yang, F., Xu, H., Wu, X., 2020. Effect of the formation of diglycerides/monoglycerides on the kinetic curve in oil transesterification with methanol catalyzed by calcium oxide. ACS Omega 5, 4646–4656. https://doi.org/10.1021/acsomega.9b04431.

Correia, L.M., Saboya, R.M.A., de Sousa Campelo, N., Cecilia, J.A., Rodríguez-Castellón, E., Cavalcante, C.L., Vieira, R.S., 2014. Characterization of calcium oxide catalysts from natural sources and their application in the transesterification of sunflower oil. Bioresour. Technol. 151, 207–213. https://doi.org/10.1016/J.BIORTECH.2013.10.046.

Da Silva, D.R., Crnkovic, P.C.G.M., Crespi, M.S., Ribeiro, C.A., 2015. Pyrolysis, combustion and oxy-combustion studies of sugarcane industry wastes and its blends. J. Therm. Anal. Calorim. 121, 309–318. https://doi.org/10.1007/s10973-015-4532-1.

Dazon, C., Witschger, O., Bau, S., Fierro, V., Llewellyn, P., 2019. Nanomaterial identification of powders: comparing volume specific surface area, X-ray diffraction and scanning electron microscopy methods. Environ. Sci.: Nano 6, 152–162. https://doi.org/10.1039/C8EN00760H.

Dietrich, R.V., 2013. Calcite. Encyclopedia Britannica. ⟨https://www.britannica.com/science/calcite⟩. (Accessed 1 July 2022).

Emeruwa, E., Jarrige, J., Mexmain, J., Bernardin, M., 1991. Application of mercury porosimetry to powder (UO₂) analysis. J. Nucl. Mater. 184, 53–58. https://doi.org/10.1016/0022-3115(91)90532-C.

Farmer, V.C., 1974. Infrared spectra of minerals. In: Farmer, V.C. (Ed.), Mineralogical, Society Monograph No. 4. Mineralogical Society, London, p. 399.

Fernandez-Diaz, L., Putnis, A., Prieto, M., Putnis, C.V., 1996. The role of magnesium in the crystallization of calcite and aragonite in a porous medium. J. Sediment Res. 66, 482–491. https://doi.org/10.1306/D4268388-2B26-11D7-8648000102C1865D.

Fujii, K., Kondo, W., 1968. Calcium glyceroxides formed in the system of calcium oxide-glycerol. With 4 figures. Z. Anorg. Allg. Chem. 359, 296–304. https://doi.org/10.1002/zaac.19683590509.

Ghiasi, M., Abdollahy, M., Khalesi, M.R., Ghiasi, E., 2020. Control of the morphology, specific surface area and agglomeration of precipitated calcium carbonate crystals through a multiphase carbonation process. CrystEngComm 22, 1970–1984. https://doi.org/10.1039/C9CE01876J.

Gregg, J.M., Bish, D.L., Kaczmarek, S.E., Machel, H.G., 2015. Mineralogy, nucleation and growth of dolomite in the laboratory and sedimentary environment: a review. Sedimentology 62, 1749–1769. https://doi.org/10.1111/sed.12202.

Gullett, B.K., Blom, J.A., Cunningham, R.T., 1988. Porosity, surface area, and particle size effects of CaO reacting with SO₂ at 1100 °C. React. Solids 6, 263–275. https://doi.org/10.1016/0168-7336(88)80066-4.

Ilgen, O., 2011. Dolomite as heterogeneous catalyst for transesterification of canola oil. Fuel Process. Technol. 92, 452–455. https://doi.org/10.1016/j.fuproc.2010.10.009.

Jazie, A., Pramanik, H., Sinha, A., Jazie, A., 2013. Egg shell as ecofriendly catalyst for transesterification of rapeseed oil: optimization for biodiesel production. Int. J. Sustain. Dev. Green Econ. 2, 27–32.

Ji, J., Ge, Y., Balsam, W., Damuth, J.E., Chen, J., 2009. Rapid identification of dolomite using a Fourier transform infrared spectrophotometer (FTIR): a fast method for identifying Heinrich events in IODP Site U1308. Mar. Geol. 258, 60–68. https://doi.org/10.1016/j.margeo.2008.11.007.

Ketcong, A., Meechan, W., Naree, T., Seneevong, I., Winitsorn, A., Butnark, S., Ngamcharussrivichai, C., 2014. Production of fatty acid methyl esters over a limestone-derived heterogeneous catalyst in a fixed-bed reactor. J. Ind. Eng. Chem. 20, 1665–1671. https://doi.org/10.1016/j.jiec.2013.08.014.

Khabbouchi, M., Hosni, K., Zidi, R., Srasra, E., 2019. Structural, conductive and dielectric properties of silicon phosphate SiP2O7 synthesis from activated clay. Appl. Clay Sci. 178, e105139 https://doi.org/10.1016/j.clay.2019.105139.

Kim, Y., Kwon, S., Roh, Y., 2021. Effect of divalent cations (Cu, Zn, Pb, Cd, and Sr) on microbially induced calcium carbonate precipitation and mineralogical properties. Front. Microbiol. 12, e646748. https://doi.org/10.3389/fmicb.2021.646748.

Kim, Y.Y., Freeman, C.L., Gong, X., Levenstein, M.A., Wang, Y., Kulak, A., Anduix-Canto, C., Lee, P.A., Li, S., Chen, L., Christenson, H.K., Meldrum, F.C., 2017. The effect of additives on the early stages of growth of calcite single crystals. Angew. Chem. 129, 12047–12052. https://doi.org/10.1002/anie.201706800.

Kirboga, S., Oner, M., Akyol, E., 2014. The effect of ultrasonication on calcium carbonate crystallization in the presence of biopolymer. J. Cryst. Growth 401, 266–270. https://doi.org/10.1016/j.jcrysgro.2013.11.048.

Kostić, M.D., Bazargan, A., Stamenković, O.S., Veljković, V.B., McKay, G., 2016. Optimization and kinetics of sunflower oil methanolysis catalyzed by calcium oxide-based catalyst derived from palm kernel shell biochar. Fuel 163, 304–313. https://doi.org/10.1016/j.fuel.2015.09.042.

Li, H., Niu, S., Lu, C., Liu, M., Huo, M., 2014. Use of lime mud from paper mill as a heterogeneous catalyst for transesterification. Sci. China Technol. Sci. 57, 438–444. https://doi.org/10.1007/s11431-013-5440-x.

Liu, D., Yates, M.Z., 2006. Formation of rod-shaped calcite crystals by microemulsion-based synthesis. Langmuir 22, 5566–5569. https://doi.org/10.1021/la060612i.

López González, L.M., Pereda Reyes, I., Dewulf, J., Budde, J., Heiermann, M., Vervaeren, H., 2014. Effect of liquid hot water pretreatment on sugarcane press mud methane yield. Bioresour. Technol. 169, 284–290. https://doi.org/10.1016/j.biortech.2014.06.107.

Luo, X., Song, X., Cao, Y., Song, L., Bu, X., 2020. Investigation of calcium carbonate synthesized by steamed ammonia liquid waste without use of additives. RSC Adv. 10, 7976–7986. https://doi.org/10.1039/C9RA10460G.

Mishchenko, V.J., Kuvardina, E.M., Loktionova, O.G., Frolova, D.A., 2012. Use of secondary resources of sugar factories. Proc. South-West State Univ. Tech. Technol. 2 (1), 274–277.

Nakatani, N., Takamori, H., Takeda, K., Sakugawa, H., 2009. Transesterification of soybean oil using combusted oyster shell waste as a catalyst. Bioresour. Technol. 100, 1510–1513. https://doi.org/10.1016/j.biortech.2008.09.007.

Ngamcharussrivichai, C., Wiwatnimit, W., Wangnoi, S., 2007. Modified dolomites as catalysts for palm kernel oil transesterification. J. Mol. Catal. A Chem. 276, 24–33. https://doi.org/10.1016/j.molcata.2007.06.015.

Nguyen, T.T., Janik, L.J., Raupach, M., 1991. Diffuse reflectance infrared Fourier transform (DRIFT) spectroscopy in soil studies. Soil Res. 29, 49–67. https://doi.org/10.1071/SR9910049.

Oche-George, P.A.O., Eras, J.J.C., Gutierrez, A.S., Hens, L., Vandecasteele, C., 2010. Residue from sugarcane juice filtration (filter cake): energy use at the sugar factory. Waste Biomass Valoriz. 1, 407–413. https://doi.org/10.1007/s12649-010-9046-2.

Paquette, J., Reeder, R.J., 1995. Relationship between surface structure, growth mechanism, and trace element incorporation in calcite. Geochim. Cosmochim. Acta 59, 735–749. https://doi.org/10.1016/0016-7037(95)00004-J.

Partha, N., Sivasubramanian, V., 2006. Recovery of chemicals from pressmud—a sugar industry waste. Indian Chem. Eng. A 48, 160–163.

Puna, J.F., Gomes, J.F., Bordado, J.C., Correia, M.J.N., Dias, A.P.S., 2014. Biodiesel production over lithium modified lime catalysts: activity and deactivation. Appl. Catal. A Gen. 470, 451–457. https://doi.org/10.1016/j.apcata.2013.11.022.

Rashid, U., Anwar, F., 2008. Production of biodiesel through optimized alkaline-catalyzed transesterification of rapeseed oil. Fuel 87, 265–273. https://doi.org/10.1016/j.fuel.2007.05.003.

Reddy, M.M., Hoch, A., 2012. Calcium carbonate nucleation in an alkaline lake surface water, Pyramid Lake, Nevada, USA. Aquat. Geochem. 18, 95–113. https://doi.org/10.1007/s10498-011-9150-3.

Remedios-Castañeiras, P.D., Wagank, A., Hailu, H.N., 2019. Characterization of biodiesel production from sugar cane filter mud oil – Wonji sugar factories in Ethiopia. Int. J. Sci. Eng. Res. 10, 1884–1851.

Rodriguez-Blanco, J.D., Shaw, S., Benning, L.G., 2011. The kinetics and mechanisms of amorphous calcium carbonate (ACC) crystallization to calcite, via vaterite. Nanoscale 3, 265–271. https://doi.org/10.1039/C0NR00589D.

Roschat, W., Siritanon, T., Kaewpuang, T., Yoosuk, B., Promarak, V., 2016. Economical and green biodiesel production process using river snail shells-derived heterogeneous catalyst and co-solvent method. Bioresour. Technol. 2016 (209), 343–350. https://doi.org/10.1016/j.biortech.2016.03.038.

Roschat, W., Phewphong, S., Thangthong, A., Moonsin, P., Yoosuk, B., Kaewpuang, T., Promarak, V., 2018. Catalytic performance enhancement of CaO by the hydration-dehydration process for biodiesel production at room temperature. Energy Convers. Manag. 165, 1–7. https://doi.org/10.1016/j.enconman.2018.03.047.

Sahebian, S., Zebarjad, S.M., Sajjadi, S.A., Sherafat, Z., Lazzeri, A., 2007. Effect of both uncoated and coated calcium carbonate on fracture toughness of HDPE/CaCO₃ nanocomposites. J. Appl. Polym. Sci. 104, 3688–3694. https://doi.org/10.1002/app.25644.

Sahu, S., Patel, B.H.M., Dutt, T., Verma, A.K., 2014. Effect of graded level of sugarcane press mud in ration on carcass characteristics of crossbred (Landrace x Desi) pigs. Indian J. Anim. Sci. 84, 1109–1112.

Sai Bharadwaj, A.V.S.L., Niju, S., Meera Sheriffa Begum, K.M., Narayanan, A., 2020. Performance and evaluation of calcined limestone as catalyst in biodiesel production from high viscous nonedible oil. Environ. Prog. Sustain. Energy 39, e13342. https://doi.org/10.1002/ep.13342.

Ševčík, R., Petr Šašek, J., Viani, A., 2018. Physical and nanomechanical properties of the synthetic anhydrous crystalline CaCO₃ polymorphs: vaterite, aragonite and calcite. J. Mater. Sci. 53, 4022–4033. https://doi.org/10.1007/s10853-017-1884-x.

Shahbandeh, M., 2022. Sugar beet production worldwide from 1965 to 2020. Statista. ⟨https://www.statista.com/statistics/249609/sugar-beet-production-worldwide/⟩. (Accessed 5 July 2022).

Shajaratun Nur, Z., Taufiq-Yap, Y., Nizah, M.R., Teo, S.H., Syazwani, O.N., Islam, A., 2014. Production of biodiesel from palm oil using modified Malaysian natural dolomites. Energy Convers. Manag. 78, 738–744. https://doi.org/10.1016/j.enconman.2013.11.012.

Shankaraiah, C., Murthy, K.N.K., 2005. Effect of enriched press mud cake on growth, yield and quality of sugarcane. Sugar Technol. 7, 1–4. https://doi.org/10.1007/BF02942519.

Shirsath, S.R., Sonawane, S.H., Saini, D.R., Pandit, A.B., 2015. Continuous precipitation of calcium carbonate using sonochemical reactor. Ultrason. Sonochem. 24, 132–139. https://doi.org/10.1016/j.ultsonch.2014.12.003.

Smith, S.M., Oopathum, C., Weeramongkhonlert, V., Smith, C.B., Chaveanghong, S., Ketwong, P., Boonyuen, S., 2013. Transesterification of soybean oil using bovine bone waste as new catalyst. Bioresour. Technol. 143, 686–690. https://doi.org/10.1016/J.BIORTECH.2013.06.087.

Syazwani, O.N., Teo, S.H., Islam, A., Taufiq-Yap, Y.H., 2017. Transesterification activity and characterization of natural CaO derived from waste venus clam (*Tapes belcheri* S.) material for enhancement of biodiesel production. Process Saf. Environ. Prot. 105, 303–315. https://doi.org/10.1016/j.psep.2016.11.011.

Thommes, M., Kaneko, K., Neimark, A.V., Olivier, J.P., Rodriguez-Reinoso, F., Rouquerol, J., Sing, K.S.W., 2015. Physisorption of gases, with special reference to the evaluation of surface area and pore size distribution (IUPAC technical report). Pure Appl. Chem. 87, 1051–1069. https://doi.org/10.1515/pac-2014-1117.

Veličković, A.V., Avramović, J.M., Kostić, M., Krstić, J.B., Stamenković, O.S., Veljković, V.B., 2021. Modeling the biodiesel production using the wheat straw ash as a catalyst. Hem. Ind. 75, 257–276. https://doi.org/10.2298/HEMIND210526028V.

Veljković, V.B., Stamenković, O.S., Todorović, Z.B., Lazić, M.L., Skala, D.U., 2009. Kinetics of sunflower oil methanolysis catalyzed by calcium oxide. Fuel 88, 1554–1562. https://doi.org/10.1016/j.fuel.2009.02.013.

Viriya-empikul, N., Krasae, P., Nualpaeng, W., Yoosuk, B., Faungnawakij, K., 2012. Biodiesel production over Ca-based solid catalysts derived from industrial wastes. Fuel 92, 239–244. https://doi.org/10.1016/J.FUEL.2011.07.013.

Xie, J., Zheng, X., Dong, A., Xiao, Z., Zhang, J., 2009. Biont shell catalyst for biodiesel production. Green Chem. 11, 355–364. https://doi.org/10.1039/b812139g.

Yadav, R.L., Solomon, S., 2006. Potential of developing sugarcane by-product based industries in India. Sugar Technol. 8, 104–111. https://doi.org/10.1007/BF02943642.

Yang, S.-D., Liu, J.-X., Wu, J., Tan, H.-W., Li, Y.-R., 2013. Effects of vinasse and press mud application on the biological properties of soils and productivity of sugarcane. Sugar Technol. 15, 152–158. https://doi.org/10.1007/s12355-012-0200-y.

Živković, S.B., Veljković, M.V., Banković–Ilić, I.B., Krstić, I.M., Konstantinović, S.S., Ilić, S.B., Avramović, J.M., Stamenković, O.S., Veljković, V.B., 2017. Technological, technical, economic, environmental, social, human health risk, toxicological and policy considerations of biodiesel production and use. Renew. Sustain. Energy Rev. 79, 222–247. https://doi.org/10.1016/j.rser.2017.05.048.